

Active solid-state nanopores: Self-driven flows/chaos at liquid-gas nanofluidic interface

Vinitha Johny[†] and Siddharth Ghosh^{†‡*}

[†]*International Centre for Nanodevices Private Limited,*

Centre for Nano Science and Engineering, Indian Institute of Science, Bangalore.

[‡]*Department of Applied Mathematics and Theoretical Physics, University of Cambridge, UK.*

We report a novel flow dynamics at the interface of liquid and gas through nanofluidic pores without applying any external driving force. Rayleigh-Taylor instability of water and air in sub-100 nanometer fluidic pores in a micrometre square domain of water and air are studied. We analyse it in the context of parameters, such as applied pressure, position to pore size ratio of the nanofluidic pore, gravity, and density. Our research also verifies the flow velocity equation with the simulation results and discuss the mass transfer efficiency of such flow structures. This is the first report on a self-driven switching mechanism of nanofluidic flow from ON to OFF or vice versa, which act as ‘active nanopore’ without any moving mechanics. A highly nonlinear complex nature of fluid dynamics is observed in nanometric length-scale, which is also one of the first studies in room temperature. Self-driven nanofluidics will have a large positive impact on biosensors, healthcare, net-zero sustainable energy production, and fundamental physics of fluid dynamics.

I. INTRODUCTION

Electrical energy harvesting from nanofluidics has been well explored [1, 2]. However, mechanical energy extraction from nanofluidics has not been explored although we have evidence that it can create large forces, which enables the flexible nanopores in stomata of the leaves to generate large negative pressure in the order of megapascal to transport water against gravity above 100 meters from the ground [3, 4]. We study this *transpirational approach* to develop a few designs suitable for very large scale integration/VLSI for on chip flow generation with application in sampling of molecules from a region of interest and nanorobotics. Besides, clean energy controlling fluid at the precision of biological cellular nanopores will bring us close to creating artificial life and next generation nanomechanically engineered transportation [5–7]. Fundamental understanding of interfacial fluid dynamics of nanometric cavities is crucial to impact nanofluidic transport mechanisms. One such approach in fluid dynamics is Rayleigh-Taylor instabilities – occurs when two fluids of different densities contact each other [8], at the interface perturbations of molecular interactions create interference patterns [9]. The rate of development of these instabilities gives insights into the fluid dynamics of interfacial systems [10]. Fluid dynamics in nanofluidic pores at the interface of liquid and gas has not been studied in depth. The limitation not only lies in experimental difficulties but also in the theoretical aspects.

Here, we present a unique self-driven flow dynamics through sub-100 nm nanofluidic pores, where the reference velocity is estimated to that in the biological nanofluidic pores of plant leaves. We use a Rayleigh-Taylor instability model at water-air interface to explain nontrivial evaporation against gravity through nanofluidic pores similar to that present in leaf surfaces. This

can also explain the rate and extend of flow with the varying densities in a system of stable solid-state nanofluidic pores with no application of external voltage or pressure against gravity. Traditionally, nanofluidic transport mechanisms are always sought to be either electrokinetically driven [11] or pressure driven [12]. However, transpiration approach of leaf has not been nanoengineered to test nanofluidic transport mechanisms. In Figure 1a, we depict such principle. The transport principle details a flow direction that diverges at the interface of the rigid wall, and the forces of van der Waals, electrostatic, induce dipole between polar and non-polar species, and oscillatory solvation pressure plays huge roles in the flow structures. We observed unique linear as well as chaotic flow patterns in a simple microreservoirs with nanofluidic pores. The velocity through the nanofluidic pore fluctuates drastically with the position of the nanofluidic pore. We report exotic fluid dynamics of 30 nm to 70 nm single and multiple nanofluidic pore systems as showed in Figure 1. Our finding opens an avenue of unexplored physics of self-driven nanofluidics and engineering opportunity of biomimicking stable nanofluidic pore flow dynamics under 100 nm for novel state-of-the-art engineering ideas at the nanoscale domain. This is the first report of a possibility to engineer active nanopores using solid-state materials. Our study raises new questions about interfacial hydraulic resistance causes stomata to close and next generation nanoengineered propulsion for transportation [13].

Model description

A nanofluidic liquid-gas interface of bulk water and bulk air is depicted with unidirectional flow patterns in Figure 1a. This system produces fluctuating incoherent flow velocities and pressures at the nanofluidic interface of water and air if the position of the nanofluidic pores is varied from edge to the centre of the reservoir as shown in Figure 1b-c. To understand this system, we coupled the

* Email of correspondence: sg915@cam.ac.uk

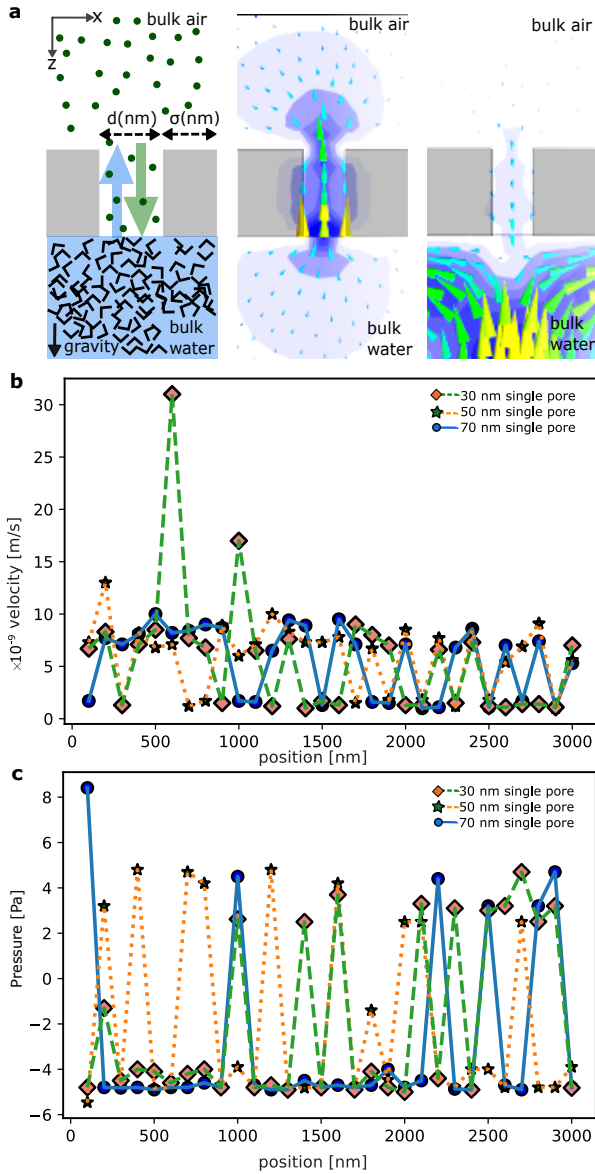


FIG. 1. (a) Principle of self-driven flow at the interface of air and water through a single nanofluidic pore; σ (nm) is the distance of nanofluidic pore from the boundary, d (nm) is the nanofluidic pore throat diameter. (b) Chaotic oscillation of reference maximum velocity in mixed phase of water and air at the interface with single pore of d of 30 nm, 50 nm, and 70 nm. (c) Variation of pressure inside the nanofluidic due to the distance from edge, σ .

continuity, momentum, and energy equations for solving the Navier-Stokes equations describing the motion of fluids. Since discretisation for structural analysis is efficient with finite element methods, we used it for simulating water-gas flow in nanofluidic pore systems in the view of the Rayleigh-Taylor instability model of fluids. We solve the flow equation and volume fraction equation. We consider volume fraction of water as 1 and air as 0 for the Eulerian modelling of multiphase flow. The general fluid

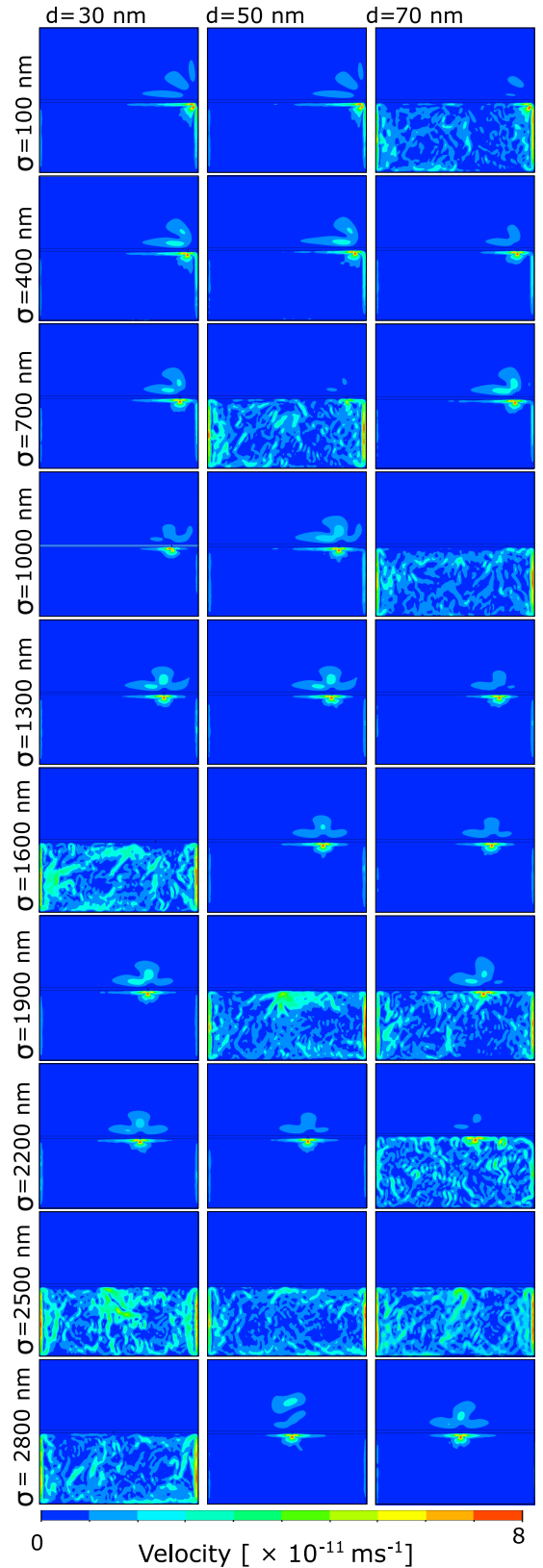


FIG. 2. Pattern of flow dynamics in bulk water and bulk air due to single nanopores by varying its diameter, d and position from the boundary, σ — column 1, column 2, and column 3 are for diameters 30 nm, 50 nm, and 70 nm, respectively. In all cases, σ is varied from the 100 nm to 2800 nm referring position from the boundary to the centre of the systems.

transport equation is given by,

$$\frac{\partial}{\partial t}(\gamma\rho\kappa) + \nabla \cdot (\gamma\rho\mathbf{v}\kappa) = \nabla \cdot \bar{\tau} + M\kappa \quad (1)$$

where γ is the phase volume fraction, ρ is the phase density, κ is the phase variable, \mathbf{v} is the phase velocity, M is the source term of added mass in the first phase dispersing to the other phase, and $\bar{\tau}$ is the diffusion term (stress tensor). This governs the flow of the system along with the volume fraction equation which is given by,

$$\frac{1}{\rho_l} \left[\frac{\partial}{\partial t}(\gamma_l \rho_l) + \nabla \cdot (\gamma_l \rho_l \mathbf{v}_l) \right] = M\gamma_l + \sum_{p=1}^n (\dot{m}_{gl} - \dot{m}_{lg}) \quad (2)$$

where \dot{m}_{gl} is the mass transfer from air phase g , to water phase l , and \dot{m}_{lg} is the mass transfer from l to g [14]. This is dependent on the mass transfer through these nanofluidic pores regardless of the direction of flow. The difference in densities of the two fluids is expected to create a pressure gradient which results in fluid flow. A fluidic reservoir of $6000 \text{ nm} \times 6000 \text{ nm}$ is separated using a 100 nm wall. This separation at the water-air interface is constituted of 96% silicon wall with the physical properties of density $2.18 \times 10^{-12} \text{ g/m}^3$, elastic modulus $6.8 \times 10^{10} \text{ Pa}$, shear modulus $2.8 \times 10^{10} \text{ Pa}$, Poisson's ratio 0.19, thermal conductivity 1.38 W/mK , and specific heat $750 \text{ J/kg}^\circ\text{C}$. The multi-phase simulation considers specific heat for air and water to be 1006.43 J/kgK and 4182 J/kgK , respectively. We used a triangular mesh geometry with an average area of $9 \times 10^{-12} \text{ m}^2$ where element mesh size is $2.5 \times 10^{-8} \text{ m}$. The viscous model is set to laminar and implicit formulation was performed. The system temperature was set to 288.16 K . The fluid dynamics for single nanofluidic pore systems with diameter, d as 30 nm , 50 nm , and 70 nm by varying the distance, σ from the boundary of the reservoir in the orthogonal direction of the gravity is shown in Figure 2. σ was varied with 100 nm steps from 100 nm from the boundary to 3000 nm in the centre. Regardless of the geometry, the interface between two fluids is considered to be linear. However, mesoscopic physics of fluidic interface is significantly complex in nanometric length scale, which is yet to be addressed. All simulations were performed in two dimensional and performed using finite element method Ansys Fluent 2021 R1 solver in Intel i7 CPU.

Single nanofluidic pore at liquid-gas interface

Although the physical model of a leaf-like system shown in Figure 1a appears geometrically simple, the fluid mechanics turned out to be non-intuitive without following a linear trend. The maximum velocity of fluid flow is expected to be at the nanofluidic interface, which should plateaued profile. However, Figure 1b and Figure 1c shows strong and random fluctuations of reference velocities and pressure. For 30 nm nanofluidic pore, by changing the position of the pore by 200 nm , we

found velocity steps of 0 ms^{-1} , $4.5 \times 10^{-9} \text{ ms}^{-1}$, and $30 \times 10^{-9} \text{ ms}^{-1}$. We observe velocity steps of 0 ms^{-1} and $10 \times 10^{-9} \text{ ms}^{-1}$ within 100 nm in $d = 50 \text{ nm}$ system. Suddenly, it shows no flow from 2500 nm to 2900 nm region and flow at 3000 nm . This strong oscillation nearly stabilises within 900 nm to 1600 nm with velocity range of $4.5 \times 10^{-9} \text{ ms}^{-1}$ to $10 \times 10^{-9} \text{ ms}^{-1}$. Then, it continues the strong oscillation over distance. Within $\sigma = 100 \text{ nm}$, 70 nm nanopore system also possess similar fluctuations, like 50 nm nanopore system. A nearly stable plateau of average $7.5 \times 10^{-9} \text{ ms}^{-1}$ can be observed within $\sigma = 200 \text{ nm}$ to 900 nm , and then continue to strongly fluctuates.

These oscillations led us to further investigate the overall flow patterns of the system. Figure 2 plots the flow patterns; the distribution of velocity magnitude over two spatial dimensions, x and y . Figure 2 shows the exemplary plots for σ varying 200 nm from previous ones – σ with 100 nm steps is shown in Supplementary Figure 6. The most common flow pattern in single nanofluidic pore systems is the cloud or hat shape with large flow velocities. The movement of the liquid through the nanofluidic pore from water phase to air phase is hindered by a back-flow as in Figure 1c and the meniscus is visible in many cases in Figure 2. In Figure 2, we observe sudden collapse of flow in the air region is found in certain positions of nanofluidic pores while varying the distance from 100 nm to 3000 nm . A driving mechanism that initiates and inhibits the flow is ubiquitous and continuous. The pressure drops above the meniscus induces a back-flow in the water to set it in motion as shown in several instances of 30 nm (at σ of 1600 nm , 2500 nm , and 2800 nm), 50 nm (at σ of 700 nm , 1900 nm , and 2500 nm), and 70 nm (at σ of 1000 nm , 1000 nm , 1900 nm , and 2500 nm). The distinct small peaks of velocity counter are observed on either side of the highest peak like that of the Gibbs-Marangoni flow [15] in Figure 2. The maximum flow rate through 30 nm , 50 nm , and 70 nm nanofluidic pores are found to be $1.3 \times 10^{-11} \text{ ms}^{-1}$, $1.3 \times 10^{-9} \text{ ms}^{-1}$, $8.4 \times 10^{-9} \text{ ms}^{-1}$, respectively when the reference flow velocity through the nanofluidic pore is set to be $4.2 \times 10^{-9} \text{ ms}^{-1}$.

In several cases, no-flow in the air phase were found while water phase possessing significant motions with strong velocity components near the boundary. We name this phenomena as ‘no-flow nano-chaos’. In Figure 2, we observed ‘no-flow nano-chaos’ in 30 nm nanofluidic pore, when it is positioned at 1600 nm , 2500 nm , and 2800 nm from the right boundary. The Appendix Figure 6 confirms more such events as it shows steps of $\Delta\sigma = 100 \text{ nm}$ — discrete events at 300 nm , 1200 nm , 2000 nm , 2300 nm , and range of this event, from 1400 nm to 1600 nm and from 2500 nm to 2900 nm . 50 nm and 70 nm nanofluidic pores do not always show ‘no-flow nano-chaos’ at same positions of 30 nm nanofluidic pore. In Figure 2, 50 nm nanofluidic pore shows this at 700 nm , 1900 nm , and 2500 nm . At $\sigma = 700 \text{ nm}$, we found transition with small flow component in the air phase. At $\sigma = 2500 \text{ nm}$, we found all cases show ‘no-flow nano-chaos’. Un-

like 30 nm nanofluidic pore, this does not show a range of positions except a short range is observed from 700 nm to 800 nm. Details from the Appendix Figure 6 confirms discrete events of ‘no-flow nano-chaos’ at 300 nm, 1700 nm, 1900 nm, 2100 nm, 2300 nm, 2500 nm, and 2900 nm. 70 nm nanofluidic pore shows ‘no-flow nano-chaos’ with small flow component in the air when it is situated 100 nm from from the boundary as plotted in Figure 2. We also see in the same figure that this occurs at 1000 nm, 1900 nm, 2200 nm, and 2500 nm. At 1900 nm and 2200 nm, transition from flow to ‘no-flow nano-chaos’ is present with strong velocity magnitude in the nanofluidic pore. In Appendix Figure 7, 1800 nm and 1900 nm shows the transient states of flow and ‘no-flow nano-chaos’. This also repeats several times in 800 nm, 1100 nm, 1500 nm, 2200 nm, and 2600 nm. Only at 1000 nm, 2500 nm, and 2900 nm, we observe pure ‘no-flow nano-chaos’. Direction of vortices and their pairs may have certain relation with the ‘no-flow nano-chaos’, we discuss this in the Discussion section. Appendix Figure 6 shows that within $\sigma = 2500$ nm to 2900 nm for 50 nm nanofluidic pore, there are three events of flow in the air phase breaking the ‘no-flow nano-chaos’, and for 70 nm nanofluidic pore in Appendix Figure 7, following similar trend like 30 nm pore, except at $\sigma = 2600$ nm, we found transition from ‘no-flow nano-chaos’ to flow in the air.

Multiple nanofluidic pores at liquid-gas interface

We have also investigated multiple nanofluidic pores systems. In Figure 8, we show flow behaviour of same geometry by increasing the number of nanofluidic pores from one to two, three, and four. We studied their spatial dependency. There are two varying cases for two pore systems based on the pore positions, such as $\sigma = (2, 4)$ μm and $\sigma = (1.5, 4.5)$ μm , and for three-pore systems, these variations are $\sigma = (0.3, 0.6, 1.5)$ μm and $\sigma = (1.5, 3, 4.5)$ μm . In case of four-pore systems, we have studied only one case with $\sigma = (1, 2.5, 3.5, 4.5)$ μm . We plot the global/complete views of velocity flow pattern with velocity vectors in the first column and its corresponding velocity stream lines in the second column of 30 nm pores (Figure 8a), 50 nm pores (Figure 8b), and 70 nm pores (Figure 8c). Followed by these global view, from fourth to seventh column represents local components of velocity vectors of local flow at the nanofluidic pores.

30 nm multipore systems: No-flow nano-chaos as well as flow are observed in two pore systems as shown in Figure 4a.oo. When $\sigma = (2, 4)$ μm , no-flow nano-chaos is prominent in the water phase. A magnified view of the pores in Figure 4a.oo($\sigma = 2$ μm) and Figure 4a.oo($\sigma = 4$ μm) show no-flow at the interface of water-air in the pores. By changing the position of two pores’ towards the nearest boundaries of the pores by 500 nm ($\sigma = (1.5, 4.5)$ μm), the system starts showing flow

from the water phase to air phase, 2.4×10^{-11} ms^{-1} and 3×10^{-11} ms^{-1} through the first and second pores, respectively. In the velocity streamlines, a synchronised global flow between two pores is observed. A magnified view of the pores in Figure 4a.oo($\sigma = 1.5$ μm) and Figure 4a.oo($\sigma = 4.5$ μm) show minor flows at the interface of water-air in the pores with significantly large flow components close to the pores in water phase. Following this observation, we have increased the number of pores to three as shown in Figures 8a.ooo. No-flow nano-chaos condition is present in three pore systems. In streamline visualisation of Figure 8a.ooo($\sigma = (1.5, 3.0, 4.5)$ μm), we found clustered flow in the centre region of the water phase. Magnified views of group of three set of pores in both cases do not show any flow component in the pore as shown in Figure 8a.ooo($\sigma = 0.3$ μm), 8a.ooo($\sigma = 0.6$ μm), 8a.ooo($\sigma = 1.5$ μm)} and Figure 8a.ooo($\sigma = 1.5$ μm), 8a.ooo($\sigma = 3$ μm), 8a.ooo($\sigma = 4.5$ μm)}). Further increasing the number of pores to four as in Figure 8a.oooo, flow is visible through all pores with clustered flow stream lines oriented towards the pores and the air phase from water to air phases. In the magnified view of these pores in Figure 8a.oooo($\sigma = 1$ μm), 8a.oooo($\sigma = 2.5$ μm), 8a.oooo($\sigma = 3.5$ μm)} 8a.oooo($\sigma = 4.5$ μm)}), the velocity vectors through every pore have an orientation towards the air phase (forward flow), and the number of pores having forward flow vectors are greater than the number of pores having backward flow vectors (towards water phase) which explains higher total flow rate towards air phase.

50 nm multipore systems: Figure 8b investigates all the same positions of 30 nm systems with change in pore size to 50 nm. The ‘no-flow nano-chaos’ systems have decreased as the pore size increased from 30 nm to 50 nm. When $\sigma = (2, 4)$ μm , the flow components are significant towards the air phase. The magnified view of these pores as in Figure 3b.oo($\sigma = 2$ μm) and Figure 3b.oo($\sigma = 4$ μm) shows a high magnitude stream of velocity vectors towards the air phase. As the position of each nanopore is changed by 500 nm towards their nearest boundaries, the flow dynamics is observed to change considerably as in Figure 8b.oo($\sigma = (1.5, 4)$ μm). In the magnified view of the pore in Figure 8b.oo($\sigma = 1.5$ μm), the flow vectors are oriented towards the water phase. Here, a reverse flow towards the water phase with magnitude of 1.5×10^{-11} ms^{-1} is observed. In Figure 8b.oo($\sigma = 4$ μm), the flow vectors takes a 2π transition towards the air phase. When the number of pores are increased to three, ‘no-flow nano-chaos’ is prominent in water phase as in Figure 8b.ooo. The magnified pore views of three pore systems of pore size 50 nm in Figure 8b.ooo($\sigma = (0.3, 0.6, 1.5)$ μm) and Figure 8b.ooo($\sigma = (1.5, 3, 4.5)$ μm) do not show any flow vectors inside the pore. Figure 8b.oooo shows evident velocity vector components through initial three pores from left boundary which tends to cease at the fourth pore. In the magnified view of these pores, Figure 8b.oooo($\sigma = 1$ μm) and Figure ($\sigma = 4.5$ μm) have flow

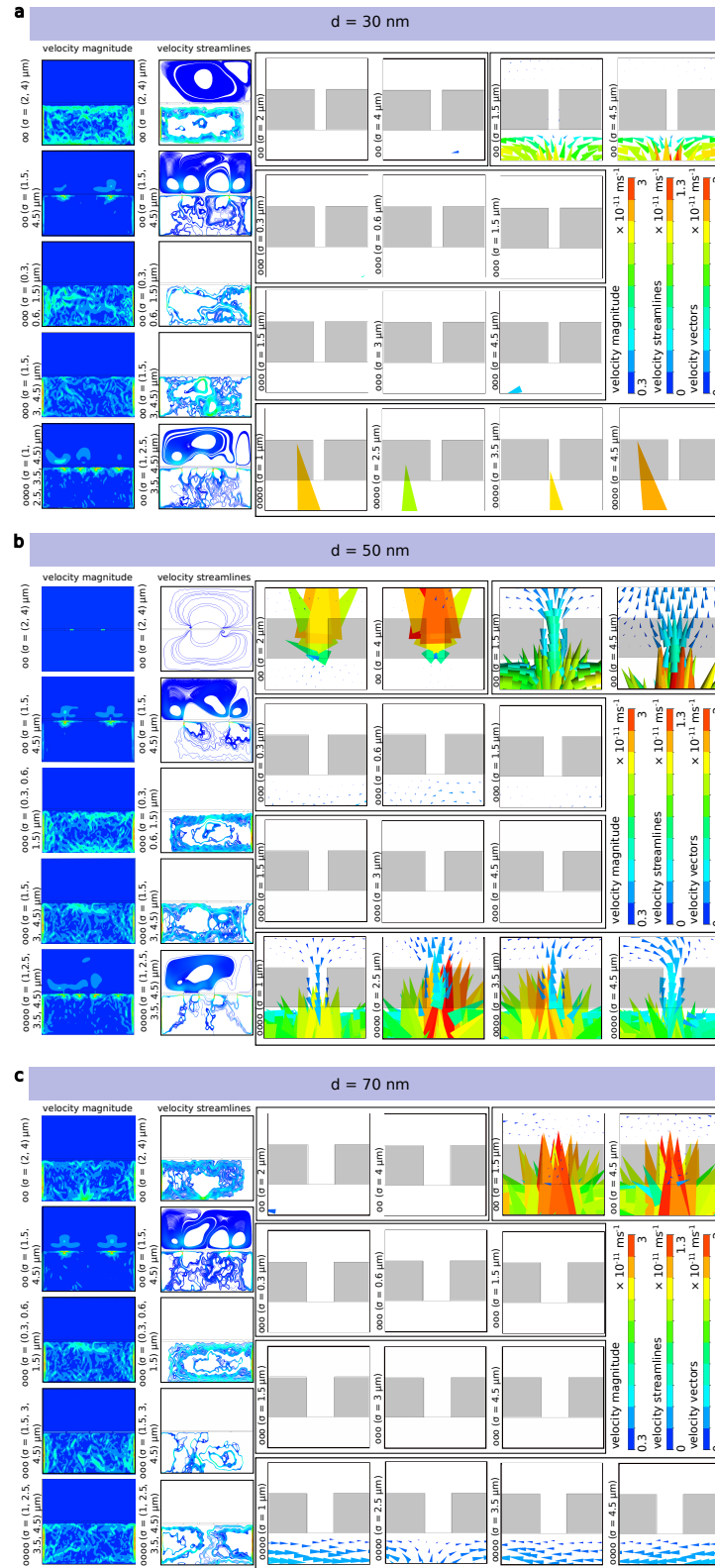


FIG. 3. **Flow patterns of multiple nanofluidic pore systems.** Global/complete views of velocity flow pattern with velocity vectors in the 1st column and its corresponding velocity stream lines in the 2nd column, and followed by these global views, 4th to 7th columns represent local components of velocity vectors of local flow at the individual nanofluidic pores in the same order of their presence from left to right in the global view. (a) 30 nm showing no prominent flow from one fluid phase to another in two pores (oo), three pores (ooo), and four pores (oooo), (b) 50 nm with two pores (oo) possessing strong flow from water to air as well as moderate flow from air to water, three pores (ooo) with no flow from different fluid phases, and four pores (oooo) showing weak flow components from one fluid phase to another, and (c) 70 nm with no flow component from one fluid phase to another in two pores (oo), three pores (ooo), and four pores (oooo)

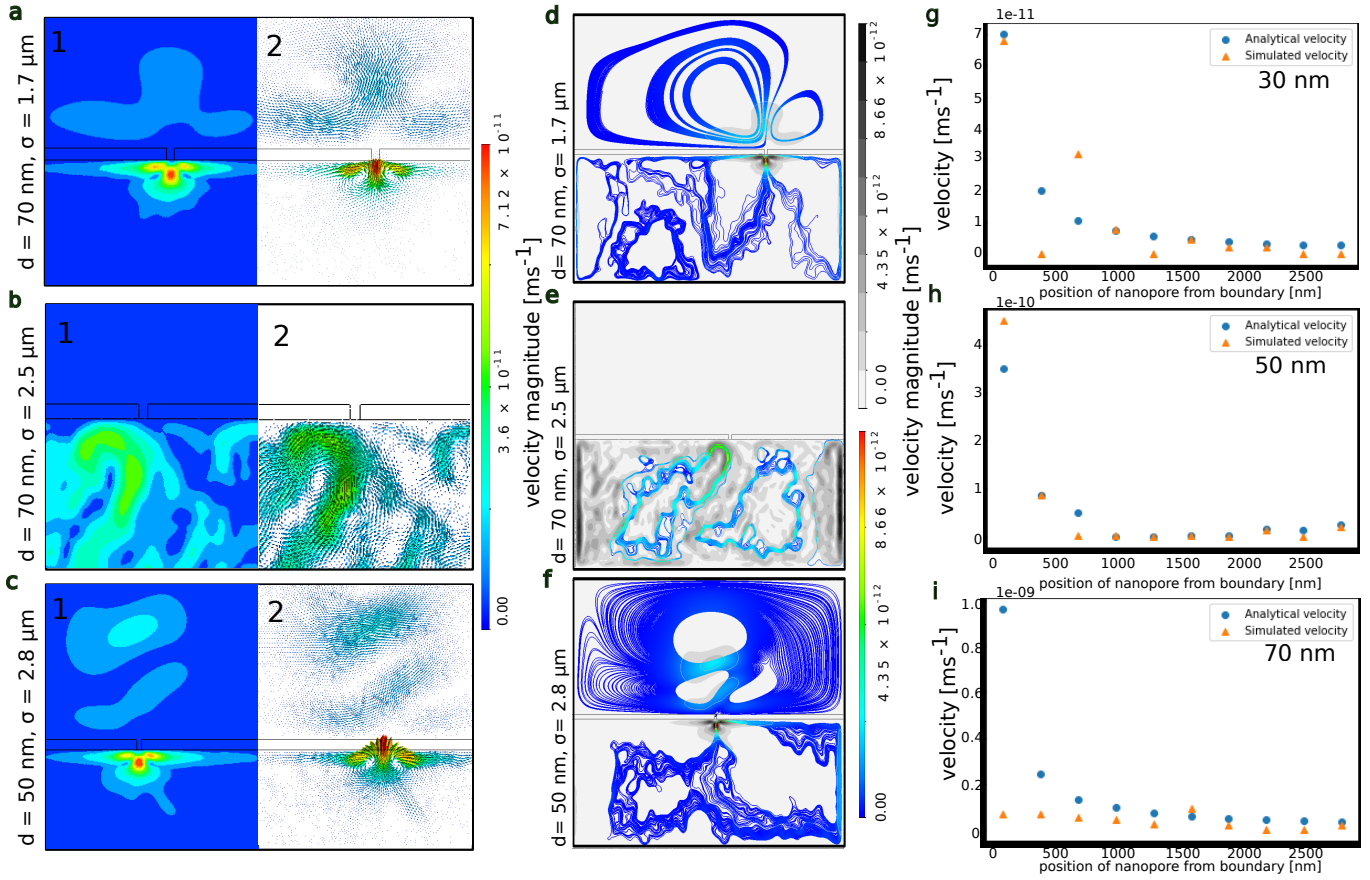


FIG. 4. **Exemplary local flow patterns at the vicinity of nanofluidic pore.** (a) Flow dynamics of single nanofluidic pore system with $d = 70$ nm situated at $\sigma = 1700$ nm; 1 – velocity magnitude distribution and 2 – velocity vectors indicating vortices in water and air resulting with no flow from water to air. Have (b) Single nanofluidic pore system with $d = 70$ nm situated at $\sigma = 2500$ nm; 1 – velocity magnitude with high value near the opening and 2 – velocity vector with no flow in air but flow component. (c) 50 nm single nanofluidic pore system at $\sigma = 2800$ nm; 1 – velocity magnitude and 2 – velocity vector with prominent back flow and vertices in water and air. **Global flow patterns and velocity streamlines in the systems for single nanopore.** (d) Complete view of (a) showing no connection of streamlines from water to air and vice versa. (e) Complete view of (b) with flow in air, significant chaotic flow patterns in air phase, and strong velocity magnitude at the boundary. (f) Complete view of (c) with the largest velocity magnitude near nanofluidic pore in water and cavitation being formed in the air phase. **Analytical and simulated mass flow velocity through nanopore as function of σ .** (g) $d = 30$ nm with prominent errors for σ at 400 nm and 700 nm (h) $d = 50$ nm with prominent errors for σ at 100 nm, 700 nm, and 1300 nm, (i) $d = 70$ nm with prominent errors in all σ except 1600 nm.

magnitude of $1 \times 10^{-11} \text{ ms}^{-1}$ towards water phase (reverse flow) and $8b.0000(\sigma = 2.5 \mu\text{m})$ and $(\sigma = 3.5 \mu\text{m})$ has flow with greater magnitude of $3 \times 10^{-11} \text{ ms}^{-1}$ and $2.7 \times 10^{-11} \text{ ms}^{-1}$ towards air phase.

70 nm multipore systems: The decrease in ‘no-flow nano-chaos’, when the pore size increased from 30 nm to 50 nm is collapsed when the pore size is further increased to 70 nm in Figure 8c. When $(\sigma = (2, 4) \mu\text{m})$, no-flow nano-chaos is prominent in the water phase. A magnified view of the pores in Figure 8c. When $(\sigma = 2 \mu\text{m})$, and Figure 8c. When $(\sigma = 4 \mu\text{m})$ show no-flow at the interface of the water-air in the pores. In Figure 8c.00($\sigma = (1.5, 4) \mu\text{m}$), the system shows maximum velocity components with magnitude of $3 \times 10^{-11} \text{ ms}^{-1}$ through the nanopore towards the air phase. A magnified view of these pores also shows minor flow com-

ponents of magnitude $0.3 \times 10^{-11} \text{ ms}^{-1}$ inside the pores towards the water phase (reverse flow). As the number of pores increased to three, there are no flow vectors inside the pores. In the magnified view of the pores in Figure 8c.000($\sigma = (0.3, 0.6, 1.5) \mu\text{m}$), there are minor flow vectors of magnitude $0.3 \times 10^{-11} \text{ ms}^{-1}$ in the water phase and, in Figure 8c.000($\sigma = (1.5, 3, 4.5) \mu\text{m}$) no flow vectors in water phase is observed. When the number of pores is increased to four, there are no flow components through any of the pores in Figure 8c.0000. In the magnified view of the pores as in 8c.0000($\sigma = 1.5 \mu\text{m}$) the velocity vectors are oriented towards the right boundary where as in $(\sigma = 2.5 \mu\text{m})$ the flow vectors diverges near the nanopore in the water phase. In Figure 8c.0000($\sigma = 3.5, 4.5 \mu\text{m}$), the flow vectors are oriented to the left boundary in the magnified view of the pore.

The change in orientation of these flow vectors are due to the divergence of flow components as observed in Figure 8c.0000 ($\sigma = 1, 2.5, 3.5, 4.5 \mu\text{m}$) of velocity streamlines.

In systems with set of four-pores, the pores have a distance of 1500 nm, 1000 nm, 1000 nm respectively between them from the left boundary. Here, a continuous and prominent flow through the nanopores are observed regardless of the change in pore size for 30 nm and 50 nm nanofluidic pore systems. Now, as the pore size increased to 70 nm and 100 nm without any change in the confined geometry, ‘no-flow nano-chaos’ was observed which is conflicting the generalization from single-pore systems. In single pore systems, as the nanopore width increased from 30 nm to 70 nm, ‘no-flow nano-chaos’ systems statistically reduced significantly for the overall simulated systems. This flow trend is manipulated with addition of identical nanopores on the silicon interface. The influence of position of pores in switching of systems with flow to ‘no-flow nano-chaos’ systems is clearly depicted in Supplementary Figure 4 as well. For two-pore systems with $\sigma = 2000 \text{ nm}$, 4000 nm , only 50 nm pore size system had prominent flow with respect to reference velocity. As the position of nanopores changed to 1500 nm and 4500 nm, respectively, the system acquired mirror symmetry across the radial axis of the geometry and prominent flow through all pores in the system was observed. Still the complete flow dynamics of multi-pore systems is unclear and needs further investigation.

Analytical approach

Let us now analytically approach validate the transport mechanism or flow structures as shown in Figure 2. We used densities of two fluids as $\rho_g = 1.225 \text{ kg/m}^3$ for air and $\rho_l = 997 \text{ kg/m}^3$ for water. Since the domain is larger than the wavelength of the instabilities, the velocity potential of the motion is given by Taylor [10] as:

$$\phi_g = Ae^{(-ky+nt)} \cos kx \quad (3)$$

$$\phi_l = Ae^{(ky+nt)} \cos kx \quad (4)$$

where ϕ_g is the velocity potential in air, A is the amplitude, k is the wave number, n is an integer, and ϕ_l is the velocity potential in water. Assuming that acceleration takes place towards the denser fluid. At the interface,

$$n^2 = -k(a_g + a_l) \left(\frac{\rho_l - \rho_g}{\rho_l + \rho_g} \right) \quad (5)$$

For example, single nanofluidic pore with diameter, $d = 30 \text{ nm}$ with maximum flow rate will have a $n^2 = -1.2 \times 10^{-6}k$. Since $(a_g + a_l)$ is positive, the instability increases with time initially until it reaches a steady state after which it is proportional to $\sqrt{\frac{\rho_l - \rho_g}{\rho_l + \rho_g}}$, which is unity in our system and explains the no flow systems. For systems without flow Equation 2 is given by

$$n^2 = 0 \quad (6)$$

In the water phase, the displacement of instability is $s = \frac{1}{2}a_g t^2$ where t is the time taken for the the steady state to achieve from the initial time, a_g is the acceleration of the molecules in gaseous phase, and v is the velocity of flow. In an evaporating liquid-gas interface, certain number of atoms/molecules condenses onto the surface of liquid. The ratio of atoms condensing to atoms evaporating is unclear and can be complicated to predict from system to system. The number of condensing molecules is a function of mean velocity through the nanofluidic pore. The number of evaporating particles is given by Feynman [16] in page 42-1 as $N = \frac{1}{\Gamma} \frac{\nu}{D} e^{(-W/k_B T)}$ where ν is the average speed of particle, W is the extra energy needed to get evaporates, k_B is the Boltzmann constant, and Γ is the cross-sectional area. Since we describe the system using continuum mechanics, we do not pursue this quantum mechanical perspective.

The vapour transport through nanofluidic pore is governed by the conventional Hagen-Poiseuille equation [17] which is given by

$$\Delta P = P_{in} - P_l = \frac{8\eta L \dot{m}}{\pi r^4 \rho_l} \quad (7)$$

where P_i is the pressure at the interface, P_l is the liquid phase pressure, \dot{m} is the mass flow rate through the nanofluidic pore, η is the viscosity of the liquid, r is the radius of the nanofluidic pore, L is the flow length, and ρ is the liquid density. Since we are addressing transport in nanofluidic pores using the Rayleigh-Taylor instability:

$$\Delta P_s = \frac{4\eta g_g t^2 \dot{m}}{\pi r^4 \rho_l} = \frac{8\eta \alpha_e N_e \dot{m}}{\pi r^4 \rho_l} \quad (8)$$

where ΔP_s is the pressure drop in simulations, α_e is the element size of the geometry used for simulation, and N_e is the number of elements in the flow region. Then the simulation velocity is given by:

$$v_s = \frac{\Delta P_s \pi r^4 \rho_l t}{8\eta \dot{m}} \quad (9)$$

Analytical form of ΔP is given by

$$\Delta P_a = \frac{4\eta v_a \sigma \Phi}{\pi r^4} \quad (10)$$

and the corresponding velocity is given by:

$$v_a = \frac{\Delta P_a \pi r^4}{4\eta \sigma \Phi} \quad (11)$$

where σ is the distance of nanopore from the boundary of the system, Φ is the area of the nanopore, ΔP_a is the pressure drop across the interface and is a constant. In Figure 4g-i, we found certain agreements between analytical and numerical velocities except in few cases large errors are observed.

DISCUSSION

In this nanofluidic study of Rayleigh-Taylor instability, we found two unique phenomena – self-driven flow and no-flow nano-chaos. In Figure 8, some velocity vectors show flow in both directions of water and air without applying any external driving force with a high probability of flow in the direction against the gravity from water to air. Figure 4a.o($d=70$ nm, $\sigma=1.7$ μm) represents the systems where the cloud of high-velocity molecules exist and the velocity vectors are pointed towards the air volume fraction. Figure 4b.o($d=70$ nm, $\sigma=2.5$ μm) represents the systems with no flow in the air and the strong back-flow in water creates vertices throughout the boundaries in the water phase. The velocity vectors show several asymmetric swirls and sudden changes in directions with a turbulent nature. In Figure 4c.o($d=50$ nm, $\sigma=2.8$ μm) represent a system with a significant flow difference pattern in the air phase. There are also cases where back-flow towards the water phase is initiated but is relatively less prominent than the velocity vectors towards the water phase. The velocity stream lines in Figure 4d.o($d=70$ nm, $\sigma=1.7$ μm) shows highest magnitude of 8.66×10^{-12} ms^{-1} at the nanopore in the water phase. When the position of nanopore changes to $\sigma=2.5$ μm , in Figure 4e.o($d=70$ nm, $\sigma=2.5$ μm) the highest magnitude of velocity streamlines is 4.35×10^{-12} ms^{-1} . In Figure 4f.o($d=50$ nm, $\sigma=2.8$ μm), the velocity streamlines are prominent through the nanopore with a magnitude of 8.66×10^{-12} ms^{-1} . In Figure 8, the velocity distribution of the multiple nanofluidic pore system become more complex than the single nanofluidic pore system. This is indicative that the molecular species in the (NVT) ensemble distribute their kinetic energy in a way to maintain the number of evaporated molecules and the number of condensing molecules in equilibrium. The vortex pairs and their vector orientation in these systems are very significant in determining net flow through the nanopores. The disruption of equilibrium at the interface and the backflow through the nanofluidic pore to the water domain may lead to the phenomenon of cavitation [18] which hinders the further flow which is not uncommon in transport through confined nanofluidic pore systems. Usually, the variations in contact angle and the liquid pressure at the interface control the evaporation process to a great extent and heat is to be supplied for it to sustain [17]. Figure 5 gives the schematic representation of self-driven flow in these system, In Figure 5a and Figure 5b, there is no net flow due to the cancellation of equal and opposite vector components. Whereas in Figure 5c and 5d, the resultant position vector is given by,

$$\mathbf{r} = b\theta + b_1\theta_1 \quad (12)$$

where b and b_1 determines the distance between the spiral loops of each spiral within the vortex pair spirals. Then Equation 13 with the correction term becomes,

$$\mathbf{v}_a = \frac{\Delta P_a \pi r^4}{4\eta\sigma\Phi} + \sqrt{\beta^2 + \omega^2 |b\theta + b_1\theta_1|^2} \quad (13)$$

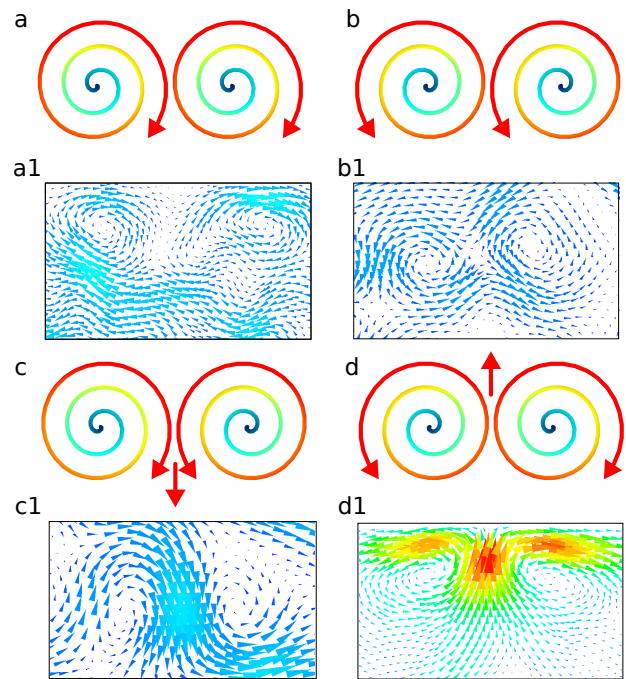


FIG. 5. **Geometry dependent pairwise-vortices driven flow.** (a) Schematic of a pair of clockwise vortices with zero resultant flow vector. (a1) Results from the simulation with pair unidirectional clockwise vortices without any resultant flow vector. (b) Schematic of pair of anticlockwise vortices with zero resultant flow vector. (b1) Results from the simulation with pair unidirectional anticlockwise vortices without any resultant flow vector. (c) Schematic of resultant flow vector for pair of clockwise and anticlockwise vortices. (c1) Simulation following the prediction in (c). (d) Schematic of strong resultant flow vector for pair of anticlockwise and clockwise vortices. (d1) Simulation showing strong resultant flow vector as depicted in (d).

and for systems with no flow, Equation 13 becomes,

$$\mathbf{v}_a = \frac{\Delta P_a \pi r^4}{4\eta\sigma\Phi} + |\beta| \quad (14)$$

where β is the constant velocity component along the perpendicular direction of nanopore throat. These vortex pairs are evident throughout every simulated system regardless of d and σ (as in Figure 5. a1 - d1).

The significant reduction in surface tension and surface conductivity in nanopores (compared to that of bulk liquid) is a frequent topic of discussion [19, 20]. The decreasing pore size to nanometre length-scale impacts the hydrogen bonding network in water as a result has lower coordination number of bonding water molecule than the bulk water [21]. Due to this enhanced affinity of water molecules for the silica surface has a large impact on the system's molecular dynamics and makes the relationship between the effects of surface tension and nanoconfinement much smaller [22]. In the modified Laplace-Young equation as in [23] which considers the solid-liquid interfacial tension, thermal energy exchange, and variation in

molecular dynamics in a nanofluidic channel, the pressure gradient of whole system has significant dependency on diameter of transport channel, and the pressure is in the range of megapascal. This changes when phase transition occurs and the nanochannel is connected to a bulk liquid, which has dimensions much greater to that of transport channel as in our case (maximum width of channel = 70 nm, maximum length of channel = 100 nm, maximum length of bulk reservoir = 6 μm). Magda et al. shows in Lennard–Jones liquid of 2-12 molecule-wide pores that the solvation force on interfacial pores of 9.5 liquid diameter wide pore are equal to the pressure of bulk liquid which is in equilibrium with the pore [24]. However, this may vary for interfacial tension of pores with smaller width less than 9.5 liquid diameter depending on the pressure [24]. Similarly, the effect of breakdown of Navier–Stokes formulations and equation of continuity on flow dynamics of microfluidic systems needs to be considered, which is addressed in a following study by us [25]. However, further study on time-dependent transient states needs to be explored for obtaining greater insight of the exact time-frames and boundary condition to determine the exact point when continuum breaks, which is highly computationally expensive and requires a separate attention. In this study, we consider the mean free path and Knudsen number as a prerequisite to the physics of the upcoming studies. We have built a basic structure of a nanoconfined system with critical values to address the physics of molecular nanofluids which is at the classical-quantum interface. Hence, at this point it may not be appropriate to generalise the results with a critical parameter or non-dimensional constant. The main objective of this study is to use computational and theoretical means to not only predict the molecular fluid dynamics but also create a potentially innovative tool of solid-state nanopore’s fluid dynamics. Our results follow the finding of Zou et al. [4] and extends it beyond the scale and capacity of their study while finding global impact of nanopores in a bulk system.

In summary, Rayleigh–Taylor instability of water and air in sub-100 nanometer fluidic pores behave in a non-trivial manner. Large flow velocities in the range of nm/s can be created through nanofluidic pores without applying any external driving force. At the same time, flow can be turned off by turning the position of the nanofluidic pores from the wall or by introducing additional pores. We have developed a fundamental understanding of nanofluidic flow dynamics by studying diverse cases in the context of parameters, such as applied pressure, position to pore size ratio of the nanofluidic pore, gravity, and density. This first report of self-driven flow and its switching mechanism will open new avenues of scientific research of the highly nonlinear complex nature of fluid dynamics at the nanometre length scale. These complex nature can be due to the co-existence of components which do not follow the conventional viscosity which can eventually head further towards the concept of coupling of an-harmonic and harmonic components in the same system at room temperature. This research will open several avenues of net-zero sustainable energy production, nanorobotic manipulation, biomolecular diagnostics, and the fundamental physics of fluid dynamics.

ACKNOWLEDGEMENTS

The authors are grateful to the internal funding of the International Center for Nanodevices. Authors are thankful to the funding provided by Honeywell Corporate Social Responsibility grant; VJ was funded by this funding. SG thanks the German Research Foundation for partly supporting this research. Professor Natalia Berloff’s scientific and mathematical opinion have found several important findings – sincere acknowledgement for this intellectual contribution in this work. The authors are thankful to Dr Moumita Ghosh for many productive discussion. Jintu K James have validated the simulations independently; we are thankful to him for that.

-
- [1] A. Siria, P. Poncharal, A.-L. Biance, R. Fulcrand, X. Blase, S. T. Purcell and L. Bocquet, *Nature*, 2013, **494**, 455–458.
 - [2] A. Siria, M.-L. Bocquet and L. Bocquet, *Nature Reviews Chemistry*, 2017, **1**, 0091.
 - [3] H. Heydt and E. Steudle, *Planta*, 1991, **184**, 389–396.
 - [4] A. Zou, M. Gupta and S. C. Maroo, *The journal of physical chemistry letters*, 2020, **11**, 3637–3641.
 - [5] A. Cheng, A. Van Hoek, M. Yeager, A. Verkman and A. Mitra, *Nature*, 1997, **387**, 627–630.
 - [6] B. L. de Groot and H. Grubmuller, *Science*, 2001, **294**, 2353–2357.
 - [7] Y. Wang, J. Cui, X. Sun and Y. Zhang, *Cell Death & Differentiation*, 2011, **18**, 732–742.
 - [8] D. H. Sharp, *Physica D: Nonlinear Phenomena*, 1984, **12**, 3–18.
 - [9] P. Linden, J. Redondo and D. Youngs, *Journal of Fluid Mechanics*, 1994, **265**, 97–124.
 - [10] G. I. Taylor, *Proceedings of the Royal Society of London. Series A. Mathematical and Physical Sciences*, 1950, **201**, 192–196.
 - [11] A. Meller and D. Branton, *Electrophoresis*, 2002, **23**, 2583–2591.
 - [12] X. Xuan and D. Li, *Electrophoresis*, 2007, **28**, 627–634.
 - [13] B. J. Yoder, M. G. Ryan, R. H. Waring, A. W. Schoettle and M. R. Kaufmann, *Forest Science*, 1994, **40**, 513–527.
 - [14] U. Manual, *Theory Guide*, 2009.
 - [15] S. Narayanan, A. G. Fedorov and Y. K. Joshi, *Langmuir*, 2011, **27**, 10666–10676.
 - [16] R. P. Feynman, R. B. Leighton and M. Sands, *American Journal of Physics*, 1965, **33**, 750–752.
 - [17] Z. Lu, S. Narayanan and E. N. Wang, *Langmuir*, 2015, **31**, 9817–9824.

- [18] J. S. Sperry, *International Journal of Plant Sciences*, 2003, **164**, S115–S127.
- [19] A. W. Knight, N. G. Kalugin, E. Coker and A. G. Ilgen, *Scientific reports*, 2019, **9**, 8246.
- [20] T. Takei, K. Mukasa, M. Kofuji, M. Fuji, T. Watanabe, M. Chikazawa and T. Kanazawa, *Colloid and Polymer Science*, 2000, **278**, 475–480.
- [21] H. S. Senanayake, J. A. Greathouse, A. G. Ilgen and W. H. Thompson, *The Journal of Chemical Physics*, 2021, **154**, 104503.
- [22] O. Galteland, D. Bedeaux, B. Hafskjold and S. Kjelstrup, *Frontiers in Physics*, 2019, **7**, 60.
- [23] Y. Qiao, L. Liu and X. Chen, *Nano letters*, 2009, **9**, 984–988.
- [24] J. Magda, M. Tirrell and H. Davis, *The Journal of chemical physics*, 1985, **83**, 1888–1901.
- [25] V. Johny, S. A. Contera and S. Ghosh, *arXiv preprint arXiv:2208.13759*, 2022.

Appendix A: Notations

σ	Position of nanopore from the reference edge
d	Diameter of the Nanopore
γ	Phase volume fraction in the multiphase flow
ρ	Phase density
κ	Phase variable
\mathbf{v}	Phase velocity
M	Mass transport through the nanopore
$\bar{\tau}$	Diffusion term/stress tensor
\dot{m}_{lg}	Mass transfer rate from phase l to phase g
\dot{m}_{gl}	Mass transfer rate from phase g to phase l
ϕ	Velocity potential
A	Amplitude of the wave
k	Wave number
a	Acceleration of the molecules
N	Number of evaporating particles from the nanopore
W	Energy corresponding to work function of evaporation
k_B	Boltzmann constant
Γ	Cross sectional area
P	Pressure
η	Viscosity of liquid
r	Radius of nanofluidic pore
L	Flow length of instability
α_e	Element size in the simulation
N_e	Number of elements in simulation
Φ	Area of nanopore
\mathbf{r}	Position vector
b	Distance constant
β	Constant velocity component in a vortex pair
(u, v, w)	Velocity components in x, y, z direction
Re	Reynolds number
E	Energy
k_{eff}	Effective thermal conductivity
suffix $_{g,l}$	Gas phase and liquid phase, respectively
suffix $_{a,s}$	Analytical and simulation, respectively
suffix $_{in}$	Interface

Appendix B: Governing differential equations

The Navier-Stokes equation holds the following governing equations to define a fluid motion. The continuity equation is given by:

$$\frac{\partial \rho}{\partial t} + \frac{\partial \rho u}{\partial x} + \frac{\partial \rho v}{\partial y} + \frac{\partial \rho w}{\partial z} = 0 \quad (\text{B1})$$

where (u, v, w) are the velocity components in (x, y, z) direction respectively, t is the time (usually a large time period is considered for steady state simulation), and ρ is the density. The momentum equation in equation B1 is given by

x -component

$$\begin{aligned} \frac{\partial(\rho u)}{\partial t} + \frac{\partial(\rho u^2)}{\partial x} + \frac{\partial(\rho uv)}{\partial y} + \frac{\partial(\rho uw)}{\partial z} = \\ -\frac{\partial p}{\partial x} + \frac{1}{Re} \left[\frac{\partial \bar{\tau}_{xx}}{\partial x} + \frac{\partial \bar{\tau}_{xy}}{\partial y} + \frac{\partial \bar{\tau}_{xz}}{\partial z} \right] \end{aligned} \quad (\text{B2})$$

y -component

$$\begin{aligned} \frac{\partial(\rho v)}{\partial t} + \frac{\partial(\rho uv)}{\partial x} + \frac{\partial(\rho v^2)}{\partial y} + \frac{\partial(\rho vw)}{\partial z} = \\ -\frac{\partial p}{\partial y} + \frac{1}{Re} \left[\frac{\partial \bar{\tau}_{xy}}{\partial x} + \frac{\partial \bar{\tau}_{yy}}{\partial y} + \frac{\partial \bar{\tau}_{yz}}{\partial z} \right] \end{aligned} \quad (\text{B3})$$

z -component

$$\begin{aligned} \frac{\partial(\rho w)}{\partial t} + \frac{\partial(\rho uw)}{\partial x} + \frac{\partial(\rho vw)}{\partial y} + \frac{\partial(\rho w^2)}{\partial z} = \\ -\frac{\partial p}{\partial z} + \frac{1}{Re} \left[\frac{\partial \bar{\tau}_{xz}}{\partial x} + \frac{\partial \bar{\tau}_{yz}}{\partial y} + \frac{\partial \bar{\tau}_{zz}}{\partial z} \right] \end{aligned} \quad (\text{B4})$$

The energy is given by

$$\frac{\partial(\rho E)}{\partial t} + \nabla \cdot (\mathbf{v}(\rho E + P)) = \nabla \cdot (k_{eff} \Delta T) + S_h \quad (\text{B5})$$

where E energy, P is the pressure, and T temperature are mass-averaged variable according to the volume of fraction model, p is phase parameter, k_{eff} is the effective thermal conductivity, S_h is the term which has contribution from radiation [14].

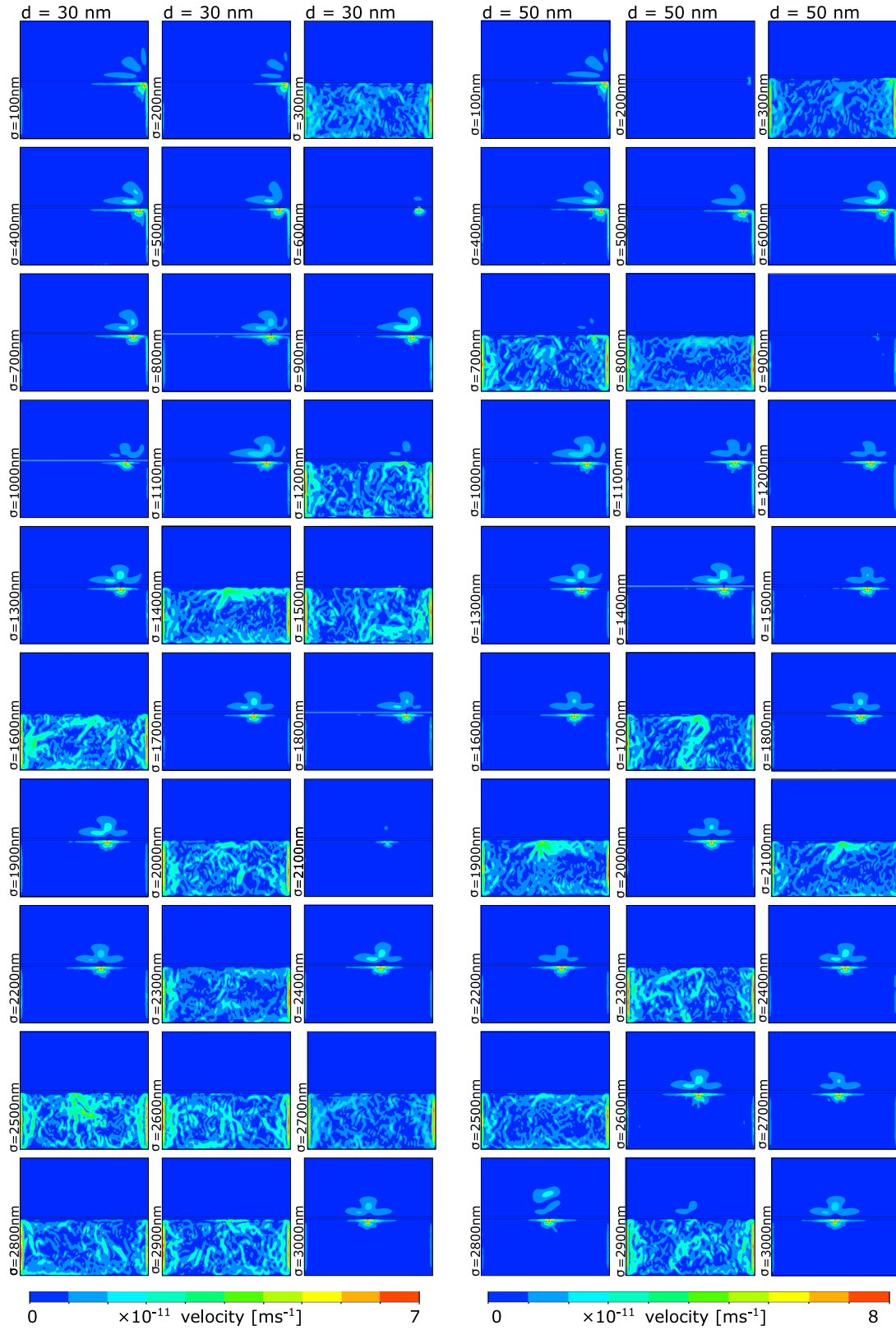


FIG. 6. Detailed flow dynamics of 30 nm and 50 nm single nanofluidic pore systems.

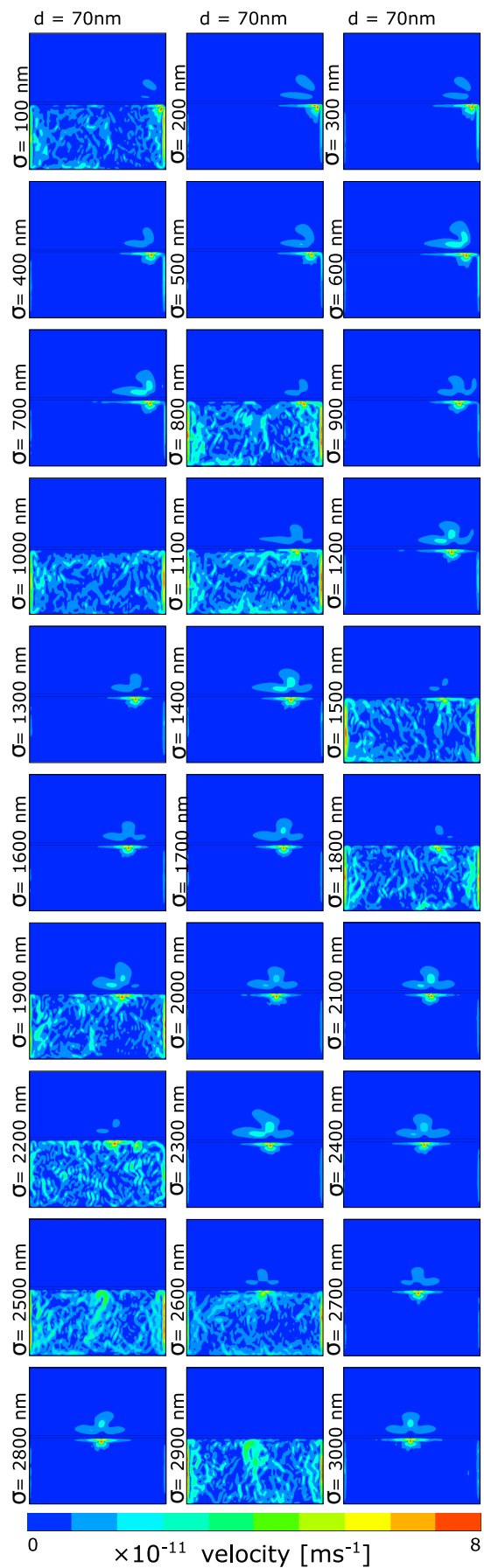


FIG. 7. Detailed flow dynamics of 70 nm single nanofluidic pore system.

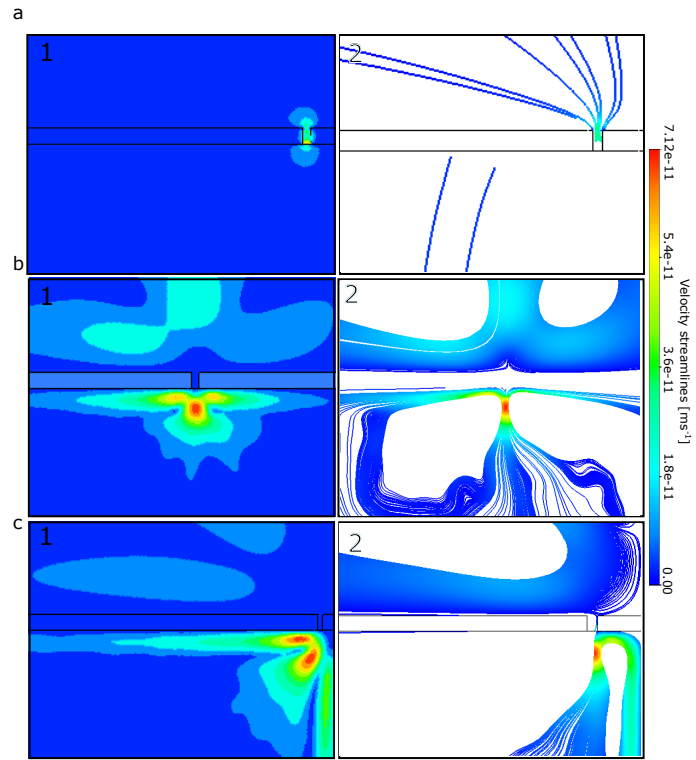


FIG. 8. (a), (b), (c) Left: Major velocity magnitude distribution patterns and right: velocity streamlines.

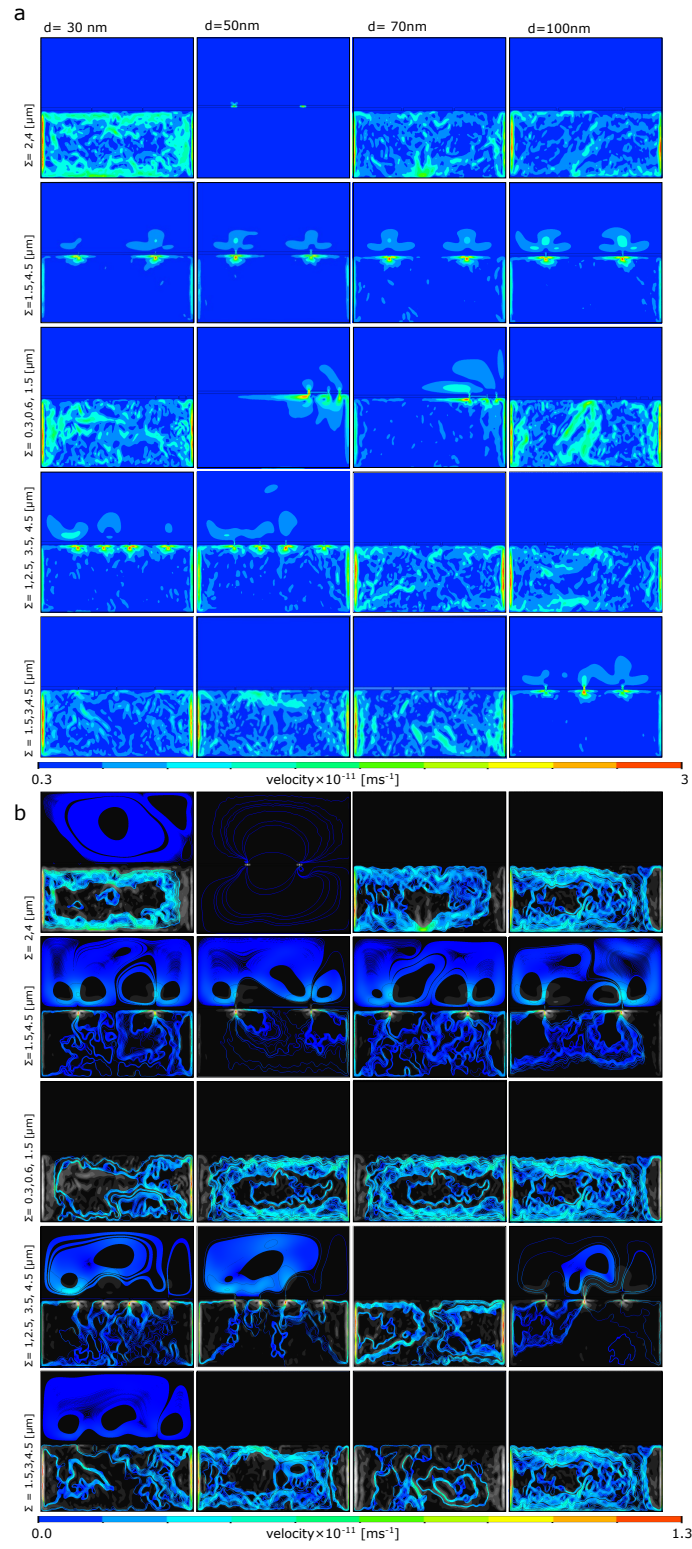


FIG. 9. (a) Velocity magnitude distribution patterns and (b) velocity streamline distribution.

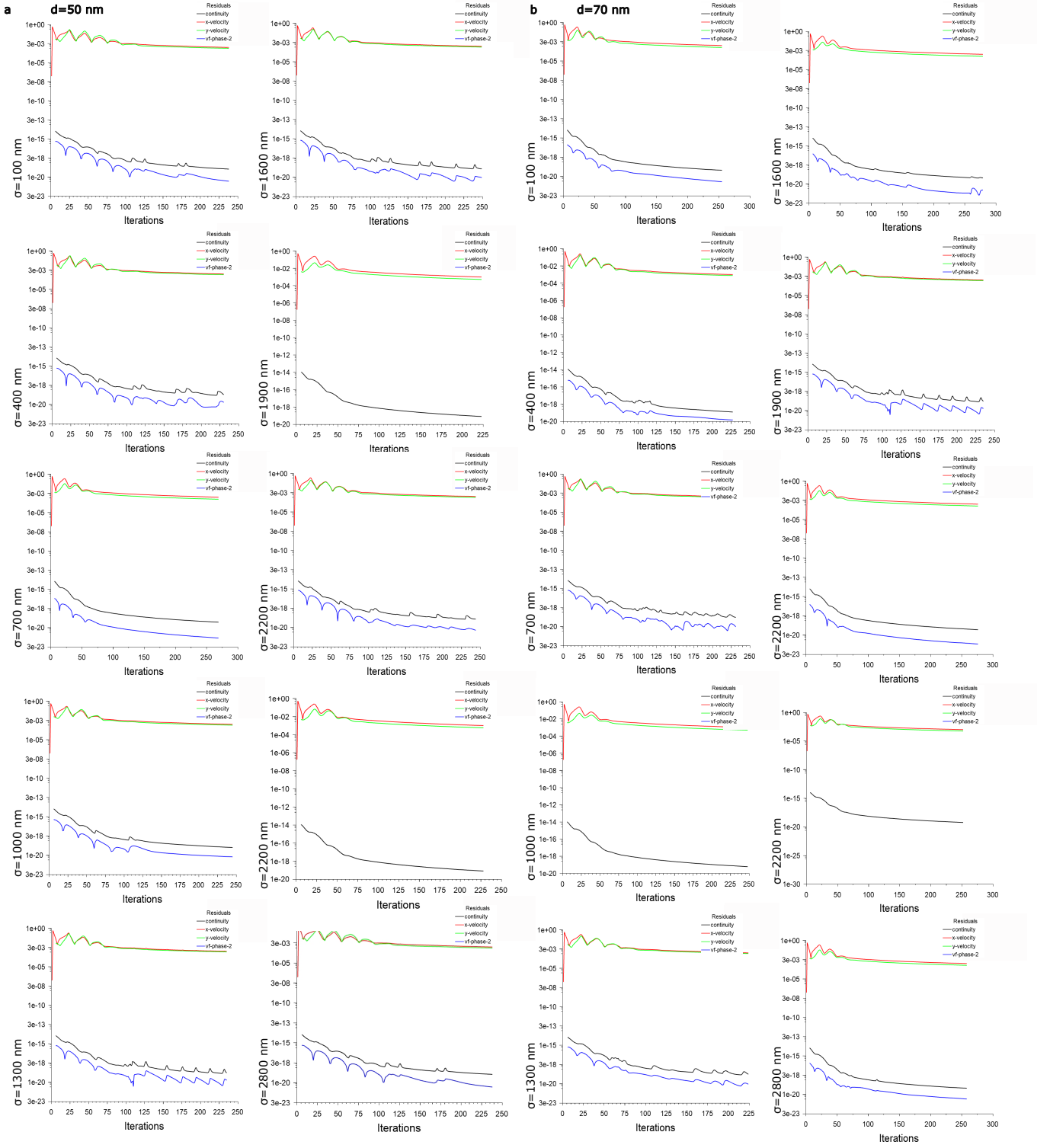


FIG. 10. absolute convergence data of residuals within the nanopore systems. (a) 50 nm pore size single nanopore systems, (b) 70 nm pore size single nanopore systems.

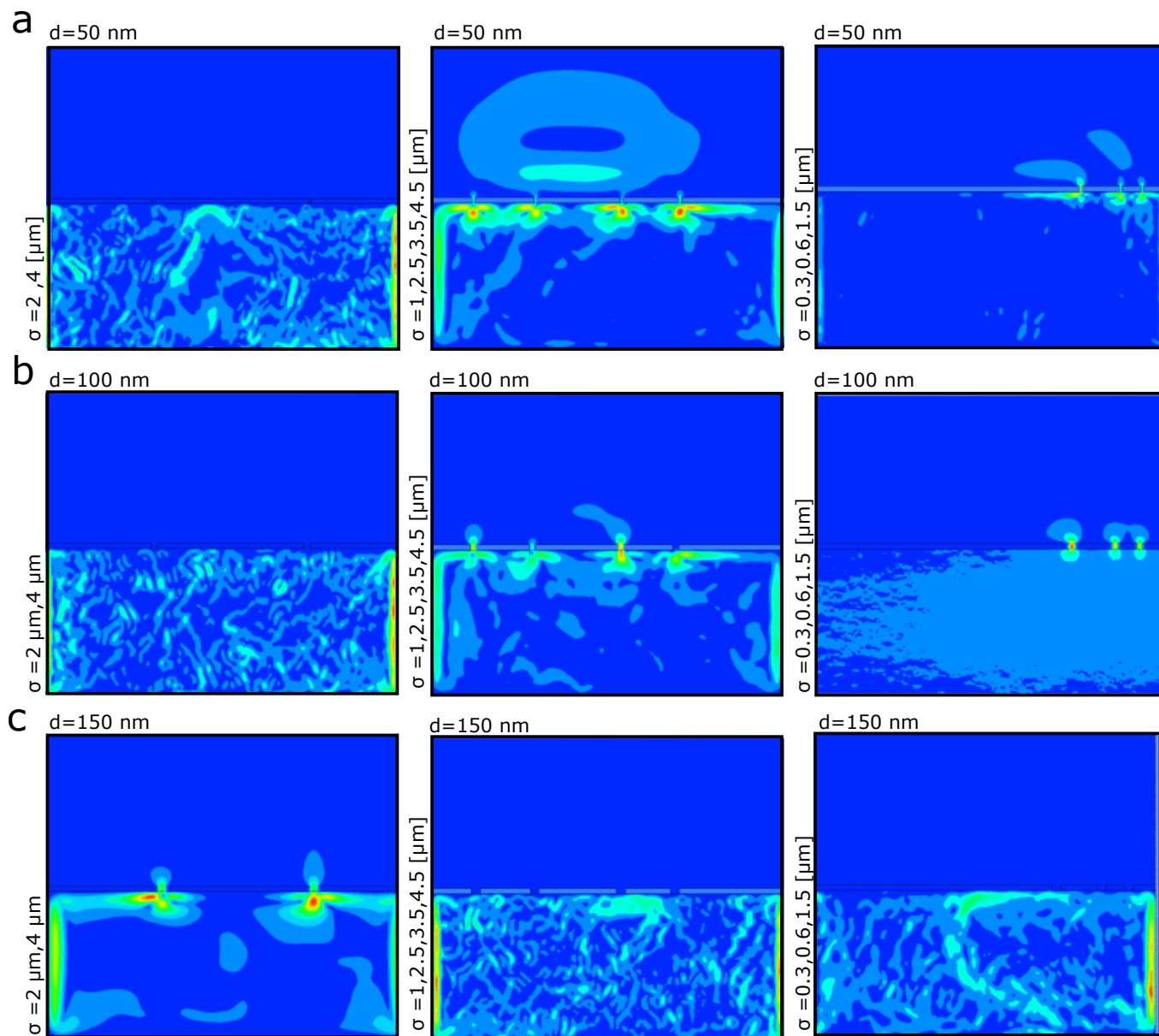


FIG. 11. Flow dynamics through the nanopores at acetone-air interface. (a) 50 nm nanopore systems with varying σ , (b) 70 nm nanopore systems with varying σ , (c) 100 nm nanopore systems with varying σ .